Science of the Total Environment 1011 (2026) 181159

Contents lists available at ScienceDirect

Science of the Total Environment

journal homepage: www.elsevier.com/locate/scitotenv

Research Paper

Learning from 3D image reconstruction: Reconstructing spatiotemporal distributions of radioactive iodine after nuclear accidents

Max Friedrich [a], Mareike Böckel [a], Oliver Meisenberg [b,*], Kathrin Meisenberg [b], Mattis Hartwig [a,c,*]

[a] *singularIT GmbH, Lübeck/Leipzig, Germany*
[b] *Federal Office for Radiation Protection (BfS), Oberschleißheim, Germany*
[c] *German Research Center for Artificial Intelligence (DFKI), Lübeck, Germany*

HIGHLIGHTS

- Reconstruction of spatiotemporal iodine distributions.
- AI-based approach as a new class of methods to reconstruct environmental contamination.
- Transferred and adapted methods from 3D image reconstruction.
- Use of indirect data such as movement profiles and thyroid iodine measurements.
- Clear impact on nuclear emergency response with transferability to other domains.

GRAPHICAL ABSTRACT

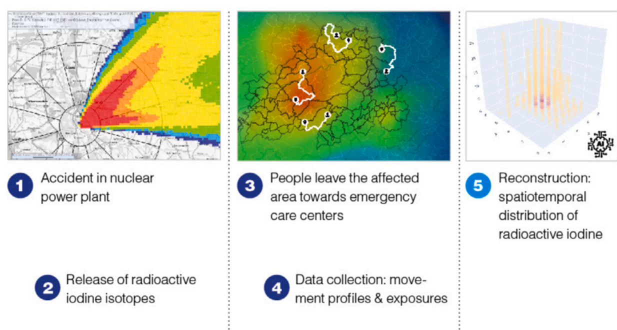

ARTICLE INFO

Keywords:
Radiation protection
Nuclear accident
Spatiotemporal reconstruction
3D reconstruction
Neural Radiance Fields
Gaussian Splatting

ABSTRACT

Determining the spatial and temporal distribution of airborne radioactive iodine isotopes is crucial for effectively managing nuclear emergencies and implementing protective measures for the population. Existing methods rely on release estimates, weather data, and dispersion models—but they do not incorporate indirect data such as measurements from affected individuals. Our research specifically focused on using innovative AI methods to incorporate movement profiles and respective thyroid iodine activity measurements of individuals in an affected area as a new data source in order to reconstruct a spatial and temporal distribution of iodine concentration in the air. To our knowledge, this is the first study to use such data for reconstructing environmental contamination fields.

In the absence of real-world emergency data, we developed a highly configurable simulator capable of generating realistic and error-prone movement profiles and related exposures. We then evaluated several AI-based reconstruction methods. The best results were achieved using Neural Radiance Fields and 3D Gaussian Splatting—state-of-the-art 3D image reconstruction techniques adapted here for environmental modeling.

Our findings show that meaningful reconstructions are possible, but depend on the amount of personal data available during an emergency. The reconstruction quality strongly depends on the ratio between spatiotemporal resolution and the number of available movement profiles: high resolution with sparse data

* Corresponding authors.
E-mail addresses: max.friedrich@singular-it.de (M. Friedrich), mareike.boeckel@singular-it.de (M. Böckel), omeisenberg@bfs.de (O. Meisenberg), kmeisenberg@bfs.de (K. Meisenberg), mattis.hartwig@singular-it.de (M. Hartwig).

https://doi.org/10.1016/j.scitotenv.2025.181159
Received 25 July 2025; Received in revised form 28 November 2025; Accepted 4 December 2025
Available online 11 December 2025

leads to increased problem difficulty and poor reconstruction results, while lower resolution combined with a higher number of paths enables more accurate and stable reconstructions.

This work introduces a new class of reconstruction methods for environmental contamination scenarios.

1. Introduction

Reconstructing the distribution of environmental contaminants from indirect measurements is a key challenge in environmental science, particularly when direct observation is limited, delayed, or infeasible. Understanding where and when people or ecosystems were exposed to pollutants is crucial for assessing long-term impacts, improving emergency response, and guiding remediation efforts.

A particularly pressing case arises in the context of nuclear power plant emergencies, where radioactive isotopes (among others iodine isotopes) are released into the atmosphere. These isotopes are transported by wind and weather, potentially exposing populations across large areas and increasing their risk of thyroid cancer (Zaletel et al., 2024). Correctly estimating the quantity of radioactive iodine in the air is essential for guiding protective actions for both affected individuals and the environment (Ishikawa et al., 2014). As an example, it can be used to assess the exposure of individuals and decide about the requirements of retroactive thyroid blocking and long-term medical follow-up (International Atomic Energy Agency, 2024).

Current methods estimate the exposure of individuals from release estimates (source term), weather data, dispersion models (typically Lagrangian particle dispersion models), radioecological models considering the precipitation of aerosol particles on surfaces, foodstuff etc., estimations regarding the intake by individuals via inhalation and ingestion, and finally biokinetic and dosimetric models. Available tools comprise among others ARGOS (PDC-ARGOS, Denmark, Hoe et al. (2009)), ESTE (ABmerit, Slovakia, Fojcíková et al. (2019)), FLEXPART (University of Vienna, Austria, and others, Stohl (2006)), HYSPLIT (NOAA, USA, Stein et al. (2015)) and RODOS ("Realtime Online Decision Support System"; KIT, Germany, Raskob et al. (2011)).

In contrast to that, our method leverages for the first time empirical data from affected individuals in the form of movement profiles and thyroid measurements. In real-life scenarios, this data is collected in emergency care centers around the affected area to assist contaminated individuals, but it has not yet been used to understand the overall environmental situation. Since the data is gathered while or after an emergency occurred, it can also be used when no other sensor infrastructure was present. Using state-of-the-art methods of artificial intelligence to combine and evaluate different sets of data that are gathered in nuclear emergencies is in accordance with the current roadmap of the European Platform on preparedness for nuclear and radiological emergency response and recovery NERIS (Challenge 4.1.3 Data assimilation/data science/artificial intelligence, Bexon et al. (2023)).

The state-of-the-art model applied in Germany is the RODOS ("Realtime Online Decision Support") system, which comprises a Lagrangian particle dispersion model taking into account the weather and the terrain as well as models for the external and internal exposure of individuals (Raskob et al., 2011, 2016). In addition to atmospheric dispersion modeling, dose reconstruction, for example of thyroid doses for the population in affected areas after a release, can also be carried out based on radiological environmental measurement data such as the local doserate from stationary and mobile measurements. In RODOS, such a dose estimation can also be carried out for individuals based on their individual movement profiles. However, there are limitations in the reconstruction of air activity concentrations, and thyroid measurements on people are also not considered. After the Fukushima Dai-ichi reactor accident in 2011, dose values for populations in affected areas were reconstructed by UNSCEAR (United Nations Scientific Committee on the Effects of Atomic Radiation) based on atmospheric dispersion modeling, radiological environmental measurement data and biokinetic modeling. However, the results of thyroid measurements carried out on people were only used for validation purposes with model results (United Nations Scientific Committee on the Effects of Atomic Radiation, 2014, 2022b,a). A numerical reconstruction of thyroid doses was conducted based on movement profiles and the results of atmospheric dispersion modeling (Ohba et al., 2020).

The German emergency plan prescribes that individuals in strongly affected areas undergo exposure measurements in emergency care centers. These measurements include an assessment of the activity of radioactive iodine isotopes, which accumulate in the thyroid. In addition, the recent movement paths of the individuals are recorded from personal interviews. This data implicitly contains information about the geospatial distribution of the atmospheric iodine concentration: A person with a high measurement value must have been exposed to a high level of radioactive iodine at one or more specific points in space and time.

In Germany, a capacity for thyroid measurements and personal interviews of at least 50 000 persons per day shall be held available according to a recommendation by the German Commission on Radiological Protection (German Commission on Radiological Protection, 2015). These measurements are conducted by emergency-response units in a number of emergency care centers, each of which shall provide measurements for 1000 persons per day over a period of ca. 10 days. Whereas after the Fukushima accident only ca. 1500 thyroid measurements were conducted (United Nations Scientific Committee on the Effects of Atomic Radiation, 2022a), more than 400 000 thyroid measurements were conducted after the Chernobyl accident (ICRP, 2020).

Currently, the available data (movement profiles and thyroid exposure measurements) are used only for the individual person, but the data sets are not combined and no general information about the environmental contamination is derived. An important research direction is to develop new methods that can incorporate this relevant source of information resulting in the following research question:

> Can the spatial and temporal distribution of iodine concentration in the air be reconstructed from the movement profiles (paths) and thyroid iodine activity measurements of individuals?

Mathematically, the desired output is a reconstruction of the iodine distribution along two spatial and one temporal dimensions based on movement profiles and thyroid iodine activity measurements of individuals as input data. Next to the atmospheric concentration of iodine isotopes at the respective location and time, several other factors influence the intake of radioactive iodine from the air and finally the result of the iodine measurement of an individual at the emergency care center: protective measures (e. g. staying inside, wearing a respiratory mask or thyroid blocking) and the age-dependent breathing rate. Additionally, excretion and radioactive decay of the iodine needs to be considered, resulting in a retention of iodine in the thyroid, which depends on the time elapsed between the intake and the measurement. The problem can be formulated mathematically as a weighted sum in the following way:

$$m_p = \sum_{i \in \mathbb{R}^3} BTS_{p,i} R_{p,i} x_i. \tag{1}$$

- x_i: Iodine concentration (isotopes 131, 132 and 133) at spacetime point $i \in \mathbb{R}^3$.
- m_p: Measured iodine activity in the thyroid at the end of an individual's path p ($p \in \{1, \ldots, n\}$ out of $n \in \mathbb{N}$ individuals).

- $S_{p,i}$: Protection factor at point i for an individual's path p. German Commission on Radiological Protection (2014, 2019)
- $R_{p,i}$: Retention factor at point i for an individual's path p. ICRP (1995)
- B: Breathing rate (constant per person).
- T: Temporal step size (constant).

The goal is to determine the iodine concentrations x_i at each spacetime point i that best explain the measured iodine levels m_p in the thyroids of individuals, given their paths and known factors B, T, S, R.

In our research, we have applied various new AI methods for this specific task of reconstructing the spatiotemporal atmospheric iodine distribution using movement profiles and thyroid iodine activity measurements. The most promising results have emerged from the application of novel 3D image reconstruction methods, namely memory-based Neural Radiance Fields (Fridovich-Keil et al., 2022) and 3D Gaussian Splatting, which we refer to as Gaussian Splatting for brevity (Kerbl et al., 2023). In line with their original purpose of reconstructing 3D objects from images, these approaches have so far been adopted in environmental modeling, with use cases ranging from the reconstruction of individual plants and other objects to the representation of entire outdoor scenes (Akhavi Zadegan et al., 2025; Rodríguez-Lira et al., 2025). To our knowledge, this is the first application of these methods to reconstruct environmental contaminant distributions—and, uniquely, to do so using movement paths rather than images.

Although the modeling in this paper focuses on the distribution of radioactive iodine isotopes, our method can be applied to a broader range of contamination scenarios. The basic scenario must contain movement profiles, a retention curve linking exposure to measured internal contamination over time and a final measurement of the individual's contamination at the end of the movement profile. Beyond nuclear emergencies, the approach could be extended to other contaminants or pollutants where people, animals, or devices traverse a contaminated zone and can be measured afterward. Thus, our approach introduces a **new class of reconstruction methods** applicable in diverse environmental pollution scenarios.

This paper is structured as follows: We first provide an overview of the data generation and the methodology including reconstruction methods, experimental setup and evaluation metrics. Afterwards, we present the key results along different experimental dimensions covering among others the number of paths, resolution of reconstruction, usage of priors and errors in the input data. Lastly, we discuss the key findings of this project and conclude with implications and suggestions for future work.

2. Data & methods

In this section we describe the generation of the dataset and all used methods for this research. Out of the five implemented methods, memory-based NeRFs (subtype of Neural Radiance Fields) and Cuboid Splatting (based on Gaussian Splatting) yielded the most promising results - both methods will be detailed here. Afterwards we describe the experimental setup and the metrics used for evaluation.

2.1. Generation of the dataset

The data for an experimental reconstruction run consist of (a) a scenario of iodine concentration in the air (b) a set of paths including thyroid iodine activity measurements and (c) a potential prior. All three components had to be synthesized, as there was no suitable data from a real emergency available. For the Fukushima Dai-ichi accident in particular, thyroid measurement data were recorded and used for the assessment of doses to the public in the UNSCEAR 2013 Report but movement profiles were not recorded (United Nations Scientific Committee on the Effects of Atomic Radiation, 2022a). In a real-world application, the scenario would be unknown, the paths and iodine activity measurements would be collected manually, and a potential prior would come from a first estimate of an iodine concentration in the air, e. g. by the RODOS system.

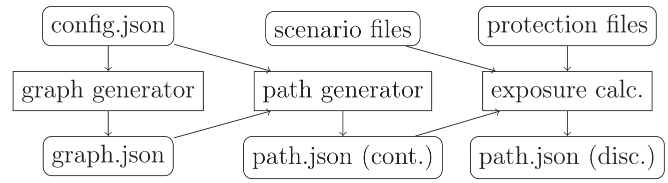

Fig. 1. Architecture of the data generator. The three sharp rectangles in the middle show the generator modules that correspond to the major generation steps. The rounded rectangles represent files that are used or generated. The config file, scenario files and protection files in the top row must be given. The graph and paths in the bottom row are generated.

In this project, four different scenarios of iodine concentration were used: Two realistic scenarios *RODOS A* and *RODOS B*, calculated with the RODOS system, and two artificial scenarios in the shape of a box in spacetime (with high contamination values) and a three-dimensional Gaussian distribution (with low contamination values).

In the scenarios *RODOS A* and *RODOS B*, typical releases of iodine from former nuclear power plant sites in Germany for the case of a major nuclear accident were assumed and real weather data were applied. However, the road networks at the regions were replaced by generated road networks. Scenario *RODOS A* was set at former Emsland Nuclear Power Plant in a flat region with source term FKF from the German source term catalog for pressurized water reactors (unfiltered containment venting, iodine release at an order of magnitude of 10^8 Bq/h for 45 h and at 10^{15} Bq/h for another 40 h, (Löffler et al., 2012)); the dispersion affected a sector of ca. 75° due to a change of the wind direction with two distinct directions of major releases during rainfall and gusty wind. Scenario *RODOS B* was set at former Gundremmingen Nuclear Power Plant in a hilly region with a variable source term of 10^{14} to 10^{17} Bq/h over 15 h; the dispersion affected a sector of 120° during dry weather and weak wind, with two directions of major releases and a wide field of smaller iodine dispersion. The dispersions were calculated over a time range of 116 h, after which the released iodine had left the region of simulation for both scenarios.

A scenario is discretized along the two spatial dimensions into 10×10, 30×30 or 100×100 cells and the temporal dimension into $1\,\mathrm{h}$ time steps. Each cell is square and has a side length of $3.84\,\mathrm{km}$ for a resolution of 100×100, $12.8\,\mathrm{km}$ for 30×30 and $38.4\,\mathrm{km}$ for 10×10.

The path data generator models the following aspects:

1. Generation of a road network.
2. Generation of groups of people (with specific characteristics and behaviors) and their movements on the road network.
3. Calculation of iodine exposures and resulting thyroid exposure measurement results for the movement profiles.

Fig. 1 shows the architecture of the generator implementation. It is a part of our experiment system and therefore implemented in Python as well. Its function is split over three modules which represent three generation stages and can be executed independently of one another, because subsequent stages reuse data generated from the earlier ones. Most data used and generated by the generators is stored as JSON files. Exceptions are for example CSV files for protection value tables.

The first stage, called the graph generator, generates a road network. The connectedness of the road network is configurable and all experiments in this paper refer to a medium level of connectedness that is comparable to a broader area with several smaller localities. Additionally, specific warning zones can be modeled for a road network, which influence the behavior of the people moving on them. All configuration options are set in one config file whose format is provided in Appendix C. The output of the first stage is a JSON file containing a road network graph.

The second stage, called the path generator, takes a road network graph and the generator config file and generates movement profiles on that graph. Per road network, individual paths of groups of people and their characteristics and behaviors were generated. Next to the location and time information, the paths contain the following aspects relevant to iodine accumulation in the thyroid: age group of the person, stable iodide tablet intake for thyroid blocking including timing and effect according to the elapsed time (Verger et al., 2001), wearing of a respiratory mask, residence indoors/outdoors / in a basement (resulting in a protection factor), moving randomly or directed towards an emergency care center or not moving, speed of movement, adhering to recommended behavior like evacuation or staying indoors in different types of warning zones or not, time difference until reaching an emergency care center (related to iodine retention) (ICRP, 1995). The output of the path generator are JSON files containing one movement profile with continuous space and time resolution each.

The third stage, called exposure calculation, takes a continuous movement profile, a scenario and protection value configuration files. It discretizes the movement profiles with respect to the scenarios resolution and annotates a protection value to each step of the movement depending on the generated circumstances in the respective profile, like taking an iodine tablet. Afterwards, it calculates the measurement value at the end of the movement profile from the protection values and the iodine distribution given in the scenario. The output of the third stage is a discrete movement profile annotated with protection values and a thyroid measurement that can be used by the reconstruction methods.

We aimed to generate realistic data by implementing a lot of configuration parameters for the generator and set reasonable values to fit realistic behavior in the generated movement profiles. All this was done to substitute the missing dataset from a real emergency as well as possible. However, we do not think that such a huge amount of realism is mathematically necessary to test if the reconstruction methods can produce good results.

The method memory-based NeRFs (details in next section) allows for a prior scenario to be loaded as part of the input data. This prior scenario can for example stem from the RODOS system with slightly different simulation parameters and is rasterized to the same resolution as the desired reconstruction.

To test for robustness of the reconstruction methods, six types of errors can be introduced to the data: exposure noise (random noise on the thyroid measurements), exposure overestimation (systematic overestimation of thyroid measurements), location variation (introduction of errors in the location data of the movement profiles), prior noise (random noise on the prior), prior rotation (systematic rotation of the prior) and prior shift (systematic displacement of the prior). All error types come with different levels of noise.

2.2. Neural radiance fields and memory-based NeRFs

2.2.1. Original method

Neural Radiance Fields (NeRFs) are neural networks that learn 3D objects from images with known camera positions and angles. They compute color and density for each 3D position and viewing direction. To render images, rays are traced through space, and colors and densities are calculated at sampled points along each ray. These colors are then weighted by density and summed to determine pixel values. Mildenhall et al. (2021) Memory-based NeRFs are a subtype of Neural Radiance Fields that directly store trained information in a data structure, such as a 3D grid, instead of relying on neural network weights and biases for computation (Fridovich-Keil et al., 2022; Liu et al., 2020). Other approaches also use data structures like trees (Rückert et al., 2022) or hash tables (Müller et al., 2022). There exist numerous variants of NeRF architectures which address various optimizations or application fields. Examples are the Mip-NeRF architectures, which extends the modeling of pixels as points and rays to pixels as 2D shapes and cones (Barron et al., 2021, 2022) or Instant-NGP which is optimized for real-time reconstructions (Müller et al., 2022).

2.2.2. Transfer

Since we are leaving the original domain of 3D reconstruction from images, we chose a relatively basic NeRF variant to test whether the method is transferable in general. Future work may try to improve our results by incorporating more specialized techniques into the method. Memory-based NeRFs apply to our case by using a 3D spacetime grid where each cell stores iodine concentration (instead of color and density values), representing its distribution over time. The paths of the individual persons in spacetime with accumulated radioactive exposure correspond to the camera rays which accumulate color values in the original method. Although those rays are straight lines in the original context of computer vision, there is no mathematical necessity in the model for these rays or paths to be straight lines. This allows us to map the concept of camera rays onto paths which in general are not straight lines. The measured exposure value at the end of a person's path corresponds to the final color value of a pixel at the end of a ray. Both of the final color values in a picture or the measured exposure along paths are calculated by a weighted sum: in the case of the image reconstruction by color values from the 3D grid structure multiplied by densities and in our use case by iodine air concentrations from the 3D grid structure multiplied by protection factors. Contrary to the density weights in NeRFs, the protection factors in our method are known and do not need to be calculated.

2.2.3. Implementation

Our adaptation of memory-based NeRFs was implemented with the PyTorch framework (Paszke et al., 2019). The iodine distribution grid is implemented as a 3D tensor, initialized at 0.0 and trained using discretized movement profiles and thyroid measurements.

The training process is based on gradient descent and iteration over training epochs. A stepwise optimization of the iodine concentration values takes place using batches of training data, mean squared error (MSE) loss function, AdamW optimizer (Loshchilov and Hutter, 2019) and learning rate scheduling. The optimization is achieved by minimizing the loss (error) between the real exposure values at the end of each path (thyroid measurements) and the reconstructed exposure values for each path based on the current state of the model (the reconstruction of the iodine distribution in spacetime). To mitigate the occurrence of overfitting, a validation set with unseen path data was introduced for selecting the final and best reconstruction among the reconstructions of all epochs. It is important to note that the original scenario is not used in the training process because it would not be known in a real-world application.

Memory-based NeRFs can optionally incorporate a prior scenario by initializing grid cell iodine concentrations with predefined values instead of 0.0. This allows integration of prior knowledge, such as RODOS system estimations, into the reconstruction.

2.3. From Gaussian Splatting to Cuboid Splatting

2.3.1. Original method

The method Gaussian Splatting is an advancement from Neural Radiance Fields in 3D image reconstruction. The approach of following camera rays from a known position and angle and accumulating color and density values along the way is the same. Unlike the NeRF-based approaches, the 3D object is not represented through a neural network or data structure but rather through the distribution of three-dimensional Gaussian distributions (Gaussians) in 3D space. These Gaussians are optimized regarding their positions in space, shapes, colors and density values so that they best represent the reconstructed 3D object. Moreover, during training, further Gaussians can be added where necessary or obsolete Gaussians can be deleted using a process called *Adaptive Density Control* (Kerbl et al., 2023).

2.3.2. Transfer

The basic idea of Gaussian Splatting is applied to our use case by representing the cloud of radioactive iodine isotopes in the three-dimensional spacetime through trainable geometric objects (original: Gaussians). Iodine concentrations in spacetime are reconstructed by calculating the overlap volume between 3D objects and the spacetime grid cells. These overlap calculations are not part of the original method (instead projections of the 3D Gaussians to 2D images happen) and are computationally costly when geometrical overlaps or probabilities for all cubic raster cells need to be calculated. Therefore the geometric object used was simplified to Cuboids, which allows for easier and more efficient computation of the overlap volumes.

These Cuboids can be trained regarding their positions, extent in spacetime and the iodine concentrations they represent. As in the original method, there is an adaptive density control mechanism, which allows to add Cuboids in so far under-reconstructed areas and to delete Cuboids whose iodine concentration sank close to zero. The transfer from camera rays to the paths of individual persons, along which they accumulate radioactive iodine when passing through the grid cells of spacetime, as well as their measured thyroid exposures is the same as for the method memory-based NeRFs.

2.3.3. Implementation

Our method Cuboid Splatting was implemented with the PyTorch framework (Paszke et al., 2019). The positions, lengths, widths, heights and iodine concentrations of the Cuboids are saved in tensors as parameters of the model. At first, a number of Cuboids (with fixed initial lengths, widths, heights and iodine concentrations) are initialized at random positions in the three-dimensional spacetime and then trained regarding their parameters based on the available training data of movement profiles and thyroid measurements.

The general approach to the training process (gradient descent, training in epochs, using batches of data, learning rate scheduler, MSE loss) and the stepwise optimization of the model are the same as for the method memory-based NeRFs. Adam (Kingma and Ba, 2015) instead of AdamW was used. The iodine concentration values of the grid cells are not directly optimized, but indirectly, by training the parameters of the Cuboids. In every epoch, the current iodine concentrations of the grid cells (current reconstruction) are calculated from the current state of the parameters of the Cuboids (current state of the model). Then, the same process of minimizing the loss between the real exposure values at the end of each path and the reconstructed exposure values for each path, based on the current reconstruction, is followed.

While it is easier to localize under-reconstructed areas in the original Gaussian Splatting application we only have the paths as an indicator where under-reconstructed areas might be located. To address this issue we adopted the adaptive density control mechanism, that has also been utilized by other researchers (Jung et al., 2024). We tested different adaptive density control mechanisms ranging from completely random to very specifically targeting under-reconstructed areas. The final implementation used to generate the experimental results presented in this publication was to identify the ten most under-reconstructed paths and randomly choose five spacetime cells where Cuboids are added. As part of the adaptive density control mechanism Cuboids get deleted if their iodine concentration values fall below a certain threshold value. Every eighth epoch, the adaptive density control mechanism takes place.

Unlike memory-based NeRFs, Cuboid Splatting showed less overfitting, allowing selection from the epoch with the lowest training error without needing a validation set (keeping in mind that we report the performance on the test set, so an additional validation set would only lead to even better results). A potential use of a prior scenario is not straightforward because of the indirect nature of the Cuboids and has not been implemented.

2.4. Experimental setup

Both reconstruction methods, memory-based NeRFs and Cuboid Splatting, were intensively evaluated in a comprehensive experimental setup. For this, the cartesian product of different experimental parameters was built to guide the experiments:

- Different numbers of movement profiles: 5000, 10 000, 25 000, partly up to 100 000
- Different spatial resolutions of the reconstructions: 10×10, 30×30, 100×100
- Different scenarios of iodine distributions (constant temporal resolution of one hour): *RODOS A*, *RODOS B*, Box, Gaussian

Even in the experiment with a spatial resolution of 10×10 for RODOS A, the scenario has roughly 10 000 spacetime cells due to the fixed temporal resolution of 116 time steps. Further experiments included additional parameters:

- The influence of using a prior scenario with the method memory-based NeRFs
- The influence of different road networks and warning zones (no consistent structural effect and thus omitted in the results)

Additionally, the effects of errors in the training data on the quality of the reconstructions were analyzed in order to examine the robustness of the methods. The experiments regarding the different types of errors described in the dataset section were carried out on a fixed parameter combination: *RODOS A* scenario, 25 000 movement profiles, 10×10 spatial resolution.

A detailed impression of the configuration file of the experimental runs is provided in the Supporting Information.

2.5. Evaluation metrics

For each spacetime cell in a scenario, we define its *overlap* as the number of paths that visited the cell during the scenario duration. Consider a natural numbered threshold count $t \in \mathbb{N}$, which we allow to be zero. We call a cell of *relevance t* if its overlap is equal or greater than that threshold. For example, all cells through which at least one path traversed are of relevance 1. This allows us to filter out all cells of the scenario where no evidence was gathered and hence no reconstruction could be made. By raising the relevance threshold further, more cells get excluded, but the average amount of evidence per included cell rises, which may contribute to a reconstruction of higher confidence. The *overlap of an experimental run* is defined as the average overlap of all cells of relevance 1 in that run's scenario.

We focus on two metrics to evaluate the performance of a specific reconstruction. The *scenario percentage error*, denoted as *% scen t rel sum* (or short in tables: scen 1 error), measures the deviation of the reconstruction from the original scenario. It is calculated over all cells with a relevance t as the proportion of the summed cell-wise absolute error relative to the summed iodine concentration of those cells. It was used as the primary error metric in the scientific development of the reconstruction methods. Since the original scenario is only available in our simulation-based experiments, but not in a real-world emergency, an additional paths-based reconstruction quality metric is needed. The *path percentage error* measures the deviation of the reconstructed exposures from the actual thyroid measurements at the end of each path in percent. It can be calculated on the set of the training paths, denoted as *% train rel sum* (or short in tables: path train), and on an unseen set of test paths, denoted as *% test rel sum* (or short in tables: path test). Training set evaluation checks if the model explains the training paths, while test set evaluation assesses generalizability. A low training error but high test error indicate overfitting.

Next to the discussed metrics, the time and memory consumption of the experimental runs as well as the progress of the training regarding the development of the loss and the learning rate were monitored.

Table 1
Percentage errors for both methods with *RODOS A* scenario, reported across different resolutions and numbers of paths.

Res.	Paths	prior	Memory-based NeRF			Cuboid splatting		
			scen 1 error	path train	path test	scen 1 error	path train	path test
10	5 k	-	91.14	0.03	29.21	37.94	4.23	17.87
	10 k		72.89	0.02	6.82	21.12	4.80	6.09
	25 k		32.98	0.05	2.15	17.74	2.75	3.70
	50 k		17.31	0.02	3.50	16.01	2.78	3.25
	100 k		13.21	0.01	0.05	16.00	2.57	3.34
30	5 k	-	121.24	0.03	282.05	125.04	4.67	104.02
	10 k		118.22	0.02	117.22	82.54	2.71	29.41
	25 k		102.83	0.21	122.02	40.14	6.37	20.83
	50 k		90.67	0.44	56.56	39.19	7.96	18.04
	100 k		53.48	0.33	23.88	25.13	3.70	3.37
100	25 k	-	131.57	0.63	982.50	145.31	31.29	89.78
	50 k		127.79	0.58	133.36	126.04	37.71	67.67
	100 k		127.20	0.26	4957.69	107.52	15.16	47.34
10	10 k	p	60.30	0.02	5.58			
30	10 k	p	96.22	0.02	98.12			
100	10 k	p	115.67	0.12	331.03			

Table 2
Percentage errors for both methods with different scenarios (all with 10 000 paths and 10×10 spatial resolution).

Scenario	Res.	Memory-based NeRF			Cuboid splatting		
		scen 1 error	path train	path test	scen 1 error	path train	path test
Box	10	16.48	0.00	0.47	0.52	0.02	0.02
Gaussian	10	79.46	0.01	7.45	18.71	2.28	3.03
RODOS B	10	32.94	0.00	0.12	62.13	4.15	3.57

3. Results

This section presents the results of our most relevant experiments, primarily focusing on the *RODOS A* scenario. Three tables summarizing the most important results have been compiled.

General results. The results in Table 1 show that implicit information in the movement profiles (paths) and thyroid iodine activity measurements about the spatial and temporal distribution of iodine concentration can be extracted by the used methods. For both methods, the ratio of the available number of training paths to the selected resolution of the reconstruction with both methods correlates with the quality of the reconstruction. If the resolution remains the same, the reconstructions improve as the number of paths increases (lower scenario and test path percentage errors). As the resolution increases, the reconstructions with the same number of paths become worse.

Quality achieved. The reconstruction of the realistic *RODOS A* scenario succeeds in the 10×10 resolution with a scenario percentage error of 13.21 % with the method memory-based NeRFs and 16.00 % with the method Cuboid Splatting, in each case with the highest number of 100 000 paths used. Even with fewer paths, e. g. 25 000, a reconstruction of the scenario is already possible at this resolution with a scenario percentage error of 32.98 % with the method memory-based NeRFs and 17.74 % with the method Cuboid Splatting. In the medium resolution 30×30, a reconstruction of the *RODOS A* scenario is still feasible, but the scenario percentage error increases to 53.48 % with the method memory-based NeRFs and 25.13 % with the method Cuboid Splatting. These values were achieved in each case with the highest number of 100 000 training paths. The quality of the reconstructions with fewer paths is lower. At the highest resolution of 100×100, even with the highest number of paths used, no suitable reconstruction of the iodine distribution of the *RODOS A* scenario is possible and the scenario percentage error exceeds 100 % with both methods. While at this resolution, the exposure values of the individual paths are reconstructed with an error above 100 % too with the method memory-based NeRFs, the method Cuboid Splatting partly still allows for path exposure reconstructions with a test path error of 47.34 %.

Results using different scenarios. The reconstruction of the other three scenarios is also generally successful. The artificial box scenario is reconstructed with the highest quality by both methods and succeeds even at the highest resolution. Particularly with the method Cuboid Splatting, the errors are very low, at <1 %. The reconstruction of the artificial Gaussian scenario is also successful with the method Cuboid Splatting in all three resolutions, with the method memory-based NeRFs only to some extent in the lowest resolution. The second realistic scenario *RODOS B* can also be reconstructed with the two methods at a resolution of 10×10 and 30×30, analogous to the realistic *RODOS A* scenario, while the reconstruction fails at the resolution of 100×100.

Influence of the choice of the reconstruction method. In comparison, the reconstructions with the method memory-based NeRFs and the method Cuboid Splatting perform similarly well in the low resolution 10×10 with a high number of paths. However, with a lower number of paths in this resolution and in the medium resolution of 30×30, the method Cuboid Splatting generally achieves the lower scenario percentage error. Remarkably, the achieved training path error with the method memory-based NeRFs is consistently very low (usually < 0.1%), while the test path error is usually (except for very good reconstructions with regard to the scenario error) considerably higher. This is different for the method Cuboid Splatting: Here, the training path error is generally higher than in comparable runs with the method memory-based NeRFs. However, the test path error is often lower and (in the case of successful reconstructions) similar to the training path error. Only in the case of a very unfavorable ratio between number of paths and resolution, the test path error is significantly higher than the training path error.

Influence of using a prior scenario. The loading of a slightly different prior scenario, implemented for the method memory-based NeRFs, leads to a significant improvement in the quality of the reconstructions by 5 to 25 percentage points reduction in the scenario percentage error. This applies to the reconstruction of both the *RODOS A* scenario and the *RODOS B* scenario with a respective prior scenario.

Influence of errors in the input data. Regarding the experiments with erroneous data, it can be observed that errors have a negative effect

Table 3
Percentage errors for experiments with erroneous data including three types of errors in different magnitudes. Tested on combination: *RODOS A*, 25 000 paths, 10×10 spatial resolution.

Noise	Memory-based NeRF			Cuboid splatting		
	scen 1 error	path train	path test	scen 1 error	path train	path test
exposure noise:						
- large	151.39	9.81	17.64	42.73	21.40	11.62
- medium	107.35	4.83	12.84	34.47	11.47	11.55
- small	45.43	0.95	4.01	29.53	4.89	5.70
exposure overestimation						
- large	40.67	0.05	19.88	31.86	3.94	21.90
- medium	88.18	2.24	7.06	50.92	11.24	17.08
- small	47.41	0.79	4.92	29.44	6.90	6.40
location variation						
- extra large	392.70	51.75	271.62	130.00	90.24	39.66
- large	278.44	28.69	33.07	79.71	49.67	20.92
- medium	247.80	8.13	25.63	66.49	24.93	17.53
- small	134.22	2.75	19.12	36.70	8.67	8.66

on the quality of the reconstructions. Low levels of random noise in the measured thyroid exposures have a less severe effect on the reconstructions than higher ones. With the systematic error in the measured thyroid exposures, the medium error level (systematic overestimation of 50% of the measurement results, vs. 10% for small and 100% for large) has the strongest negative effect for both methods. Errors in the location information of the movement profiles have the strongest deteriorating effects for both reconstruction methods. The introduction of errors into the loaded prior scenario for the method memory-based NeRFs has almost no negative effect on the reconstruction results (excluded from the tables as no effect is observable) and still leads to better results than the comparable reconstruction without prior scenario.

A comparison of the results of the two methods shows that the method Cuboid Splatting achieves considerably better reconstruction qualities with erroneous data than the method memory-based NeRFs. Further, the test path error of the method Cuboid Splatting is often lower than the training path error in the case of erroneous and therefore contradictory training data (but error-free test data). However, the test path error is consistently higher than the training path error with the method memory-based NeRFs.

Influence of warning zones and different road networks. When warning zones were declared in the affected area (tested using the RODOS A scenario), this generally had a positive effect on the reconstructions using both methods, memory-based NeRF and Cuboid Splatting, and frequently resulted in lower scenario percentage errors. Especially noteworthy are the reconstructions with the method Cuboid Splatting in the resolution 30×30, where with lower path numbers the error for comparable runs without warning zones was very high and with warning zones fell to only a fraction of this error. The experiments also considered the impact of different road networks. All results in the presented tables refer to the “Villages” road network. Additional results with other road networks are provided in Fig. D.7. Overall, the following showed: The underlying road network (main roads, villages or city) can slightly affect the quality of the reconstructions but there is no clear trend indicating which road network leads to particularly good or poor reconstructions. Similar general trends are observed across all road networks, such as improved reconstructions with an increasing number of paths.

Time and memory requirements of reconstructions. Time and memory consumption of experimental runs increase with resolution, number of training paths, and epochs for both methods. Cuboid Splatting is faster at lower resolutions, with 10×10 runs taking up to 120 min. At higher resolutions like 30×30 and 100×100, the time extends to 12 and 36 h, respectively. High-resolution training runs (100×100) often had to stop early due to memory constraints on a 6 GB RAM laptop GPU. Memory-based NeRFs reconstructions take between 4 and 24 h. No memory constraints were encountered in experiments with this method.

4. Discussion

In this section, we discuss our key findings and implications for the field of radiation protection.

4.1. Key finding 1: Both methods are fundamentally suitable for solving the problem

The results (presented in Tables 1 and 2) show that both methods, memory-based NeRFs and Cuboid Splatting, are fundamentally suitable for extracting meaningful information from movement profiles and thyroid measurements, enabling the reconstruction of iodine distributions in spacetime. This is evidenced by the achieved reconstruction qualities of the different scenarios presented above. A prerequisite for this is the availability of a sufficient amount of training data, which are the thyroid measurement results and movement profiles of the persons that attend an emergency care center.

Reconstructions at a lower resolution (10×10) are particularly successful. Reconstructions at a medium resolution (30×30) are also feasible. However, reconstructions at a high resolution (100×100) have not yet been successful.

The simple form and sharp boundary between high iodine concentrations in the Box scenario compared to unaffected areas are the easiest to reconstruct for both methods. The Gaussian scenario, due to its continuous shape in spacetime, is well reconstructed using the Cuboid Splatting method. The more complex shapes of realistic scenarios (*RODOS A* and *RODOS B*), which feature very high iodine concentrations in certain locations and lower concentrations in others, are more challenging to reconstruct and require more training data.

4.2. Key finding 2: The number of paths and the overlap play a central role for the reconstructability

Fig. 2 demonstrates a clear trend between the paths-to-resolution ratio and reconstruction quality, revealing that path overlap in spatiotemporal cells is crucial for accurately reconstructing iodine distributions. When multiple training paths intersect in a given cell, the model must assign an iodine concentration that satisfies all these paths. As a result, the model cannot arbitrarily distribute iodine along any single path, making the resulting concentration more likely to generalize beyond the training data. Moreover, having more paths could have an additional positive effect as it increases the diversity of information, because different paths overlap at different points, leading to a more comprehensive capture of overarching iodine distribution patterns.

In practical terms, this finding suggests that the chosen reconstruction resolution should align with both the available training data (i.e., the number of paths) and the required level of reconstruction quality. Together these numbers correspond to the overlap of the scenario.

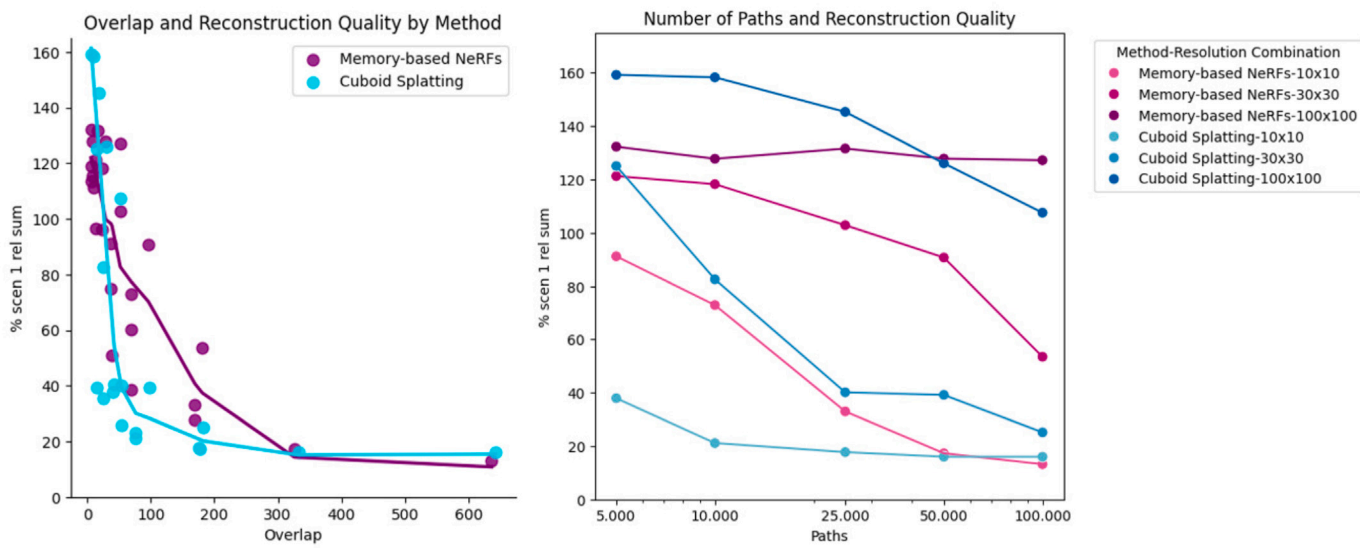

Fig. 2. Left: Overlap compared to scenario error for both methods with LOWESS trendline. A higher overlap between paths leads to higher reconstruction quality. Right: Relationship between number of training paths and scenario error. A trend of more paths leading to higher reconstruction quality is observable. (*RODOS A* scenario)

4.3. Key finding 3: While memory-based NeRFs tend to overfit, cuboid splatting rather learns generalizable and overarching patterns

The significant difference between the training path error and the test path error in the method memory-based NeRFs indicates a tendency towards overfitting. While the model can accurately reconstruct the training data, it sometimes struggles to generalize well to unseen data, resulting in worse reconstructions. This issue is less pronounced in the Cuboid Splatting method, which achieves better generalizable reconstructions even with less overlap.

We explain the better performance of Cuboid Splatting by the fact that the reconstructed iodine exposures of two paths are already correlated if the two paths pass through the same Cuboid. This does not require an explicit overlap in a single spacetime cell, the paths can also pass through nearby cells. In contrast, with memory-based NeRFs, an explicit overlap is required for the exposures of two paths to be related. Therefore, while memory-based NeRFs only learn the iodine concentrations of individual spacetime cells, Cuboid Splatting rather learns the overarching patterns of iodine distribution in spacetime. Fig. 3 illustrates the learning of broader structures (blue cubes on the right) by the Cuboid Splatting in contrast to learning each spacetime cell individual (dots on the left) by the NeRF approach.

This characteristic enables Cuboid Splatting to combine lower overlaps in some cells into higher overlaps per cuboid. It also explains the higher robustness of Cuboid Splatting to data errors, as it can better compensate for errors with more contrasting evidence. While memory-based NeRFs' reconstruction quality significantly suffers from errors, Cuboid Splatting can comparatively better create generalizable models despite training data errors.

4.4. Key finding 4: Loading a prior scenario improves the reconstruction

Incorporating prior knowledge from other data sources (a prior scenario) in the method memory-based NeRFs significantly improves reconstructions (see Table 1) and thus should be utilized whenever possible. Interestingly, even flawed priors lead to better reconstructions than none, suggesting their use despite doubts about their quality. However, further investigation is needed to determine if the improvement is due to prior knowledge or just non-zero initialization, which was not explored in the experiments. Furthermore, developing a mechanism to integrate prior knowledge into the method Cuboid Splatting is advisable, as a similar enhancement effect is possible.

4.5. Key finding 5: Certain error levels in the inputs are tolerable, but the greater the inconsistencies, the worse the reconstructions

As shown in Table 3, the methods demonstrate a certain tolerance to errors in the input data, such as minor inaccuracies in thyroid measurements, allowing for slightly less accurate yet feasible reconstructions. However, the reconstruction quality significantly deteriorates with increasing contradictions in the training data. Errors in movement profiles have the most detrimental impact, suggesting the consideration of alternative, more accurate data collection methods, such as using movement data from smartphones or smartwatches instead of self-reported data. As previously mentioned, Cuboid Splatting has shown itself to be more robust than memory-based NeRFs against erroneous data. Cuboid Splatting even manages to balance out some of the errors in the training data, as evidenced by a lower test path error compared to training path error.

5. Conclusion

Our findings demonstrate that the spatial and temporal distribution of iodine concentration in the air can indeed be reconstructed from individual movement profiles and thyroid iodine activity measurements with methods from 3D image reconstruction. By harnessing the implicit information within these previously untapped data sources, we are the first to show that they can serve as an additional data source for spatiotemporal reconstruction of atmospheric iodine concentration.

When the movement profiles are used as a full substitute for all other common methods, the quality of the reconstruction is limited in higher resolutions. Coarse spatiotemporal reconstructions of radioactive iodine distributions after nuclear accidents at 10×10 or 30×30 grids can be fully solved with a realistic number of movement profiles. Although reconstructions on these coarse resolutions are not sufficient to determine the iodine concentration on their own, they can be applied as additional data to improve the results of highly resolved dispersion simulations like RODOS as it is also the case with environmental measurements (data assimilation, Rojas-Palma et al. (2003)).

High-resolution reconstructions (e.g., 100×100) remain challenging with movement data alone, as our current simulations indicate. Future research should explore to combine existing simulation approaches with the reconstruction methods presented in this paper, since in reality the movement profiles are an *additional* source of information

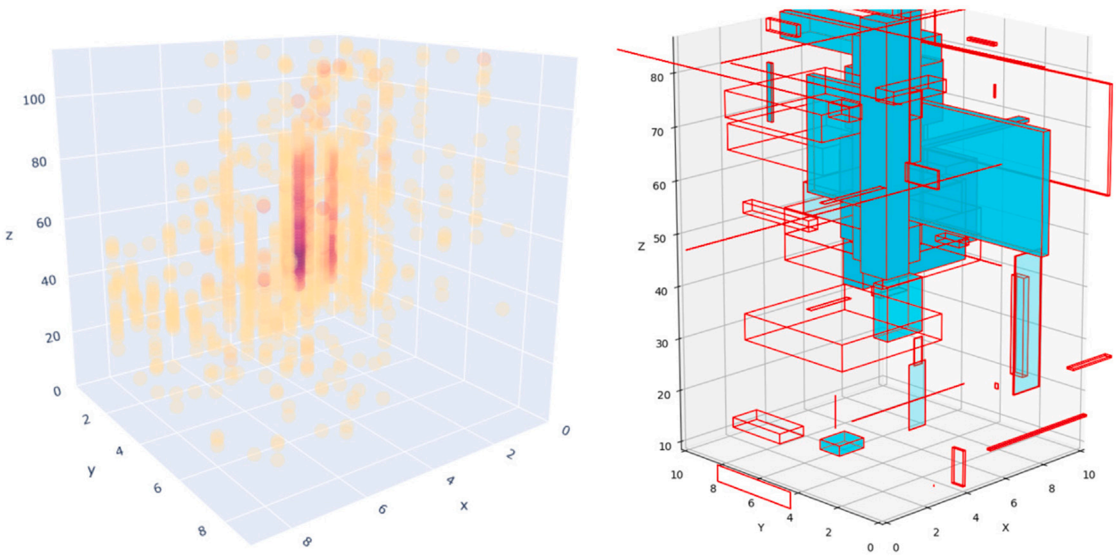

Fig. 3. Model representations of memory-based NeRFs (left) and Cuboid Splatting (right). The y-axis and the x-axis represent the two spatial dimensions, whereas the z-axis represents the time dimension. While the NeRF model directly learns the iodine concentrations of spacetime cells represented by the dots on the left (yellow = small concentration, purple = high concentration), the Cuboid model learns overarching 3D-structures (blue saturation of the cuboids represents the levels of iodine concentrations) and thereby has a lower tendency to overfit.

and not necessarily a substitute. Approaches such as integrating air measurements and weather dispersion models into the presented reconstruction methods, researching best ways to handle priors (also in Cuboid Splatting) as a way to insert prior knowledge, or adopting adaptive resolution schemes could reduce the number of required paths while improving reconstruction fidelity.

In addition to methodological advances, future policy research should also consider how to maximize the availability of movement path data. Aggregated mobility data from mobile phone providers or dedicated exposure-tracking applications might be a promising first step towards making large-scale path data accessible in practice.

We believe that our approach generalizes well beyond nuclear emergencies and introduces a new class of reconstruction techniques for environmental contamination scenarios. Apart from modeling the impact of protective measures, both our theoretical modeling and most of the implementation are designed to be applicable to other forms of environmental contamination. Future research should focus on demonstrating this transferability through concrete case studies involving different types of contaminants or exposure settings.

CRediT authorship contribution statement

Max Friedrich: Writing – review & editing, Writing – original draft, Visualization, Validation, Software, Methodology, Formal analysis, Data curation, Conceptualization. **Mareike Böckel:** Writing – review & editing, Writing – original draft, Visualization, Validation, Software, Methodology, Conceptualization. **Oliver Meisenberg:** Writing – review & editing, Supervision, Project administration, Methodology, Investigation, Funding acquisition, Conceptualization. **Kathrin Meisenberg:** Writing – review & editing, Supervision, Project administration, Methodology, Investigation, Funding acquisition, Conceptualization. **Mattis Hartwig:** Writing – review & editing, Writing – original draft, Validation, Supervision, Project administration, Formal analysis, Conceptualization.

GenAI disclosure

Since the authors of this paper are all not native english speakers, we used AI-tools to improve our spelling, grammar and formulation. This was done to improve readability and ease the experience for the reader.

Declaration of competing interest

The authors declare that they have no known competing financial interests or personal relationships that could have appeared to influence the work reported in this paper.

Acknowledgments

This study was supported by the Federal Ministry for the Environment, Climate Action, Nature Conservation and Nuclear Safety, Germany under contract 3622S62583. The study's contents are solely the responsibility of the authors.

Appendix A. Code

The research code will be published soon in the following code repository: https://github.com/OpenBfS/iodine-reconstruction.

Appendix B. Literature review on reconstruction methods, selection criteria and selection results

In the beginning of the research project, a literature search was carried out to identify potential reconstruction methods. Each identified method was evaluated for its transferability to the use case and assessed based on selected criteria.

The literature search was carried out as a keyword search in several search engines (*Google Scholar*, *Papers With Code*). In a second iteration, we supplemented our search results with references from citations of the found literature, meta-studies, and encyclopedias. Next, we evaluated each method's transferability to modeling different parts of our problem: the distribution of iodine in the atmosphere, the intake of iodine by a person along their path and the measured exposure value at the end of a person's path. Methods that could not be applied to all parts of the problem were excluded. We evaluated the identified and non-excluded methods based on the following weighted criteria, each criterion defined by one or more relevant questions. Weights were based on a criterion's importance.

1. Similarity (weight: 4): How similar are our problem and the problems solved with the method Can we transfer the method to our problem with reasonable effort?
2. Time requirements (weight: 4): How much computing power and thus time does the method require? Can the method be carried out with the given expected problem size in the desired time on the desired end device?
3. Memory requirements (weight: 4): How much memory does the method require? Can the method be executed with the given expected problem size with the desired memory requirement on the desired end device?
4. Data requirements (weight: 4): How much training data is required? Can the method extract a meaningful solution from the given amount of data? Can the method produce usable results even with little data?
5. Uncertainty (weight: 3): Can the method evaluate the reconstruction with an uncertainty, for example a variance?
6. Robustness (weight: 3): How well can the method handle erroneous data? How strongly does the method react to fluctuations in inputs?
7. A priori capability (weight: 2): Is it possible to incorporate prior knowledge? Is the introduction of prior knowledge necessary? We consider the following forms of prior knowledge about the problem: prior knowledge about the state of individual data points, e.g., through on-site measurements, prior knowledge about an approximate form of the solution, e.g., through simulations, assumptions about the form of the solution, in particular with regard to sparsity and smoothness.
8. Implementation effort (weight: 2): How much implementation is necessary? We evaluate the effort for two parts in particular: Core of the method and preparation of the data to apply the method to. Are there libraries or frameworks that simplify implementation?
9. Maturity (weight: 1): How well researched is the method?
10. Popularity (weight: 1): In which areas is the method used?
11. Range of application (weight: 1): How diverse are the areas of application of the method?

The evaluation results for the methods (ordered from highest to lowest score) are the following:

1. Stochastic Robust Optimization (Boyd et al., 2004) - Score: 111/145
2. Bayesian Inverse Problems (Dashti and Stuart, 2017) - Score: 111/145
3. Linear Optimization (Vanderbei et al., 2020) - Score: 95/145
4. Gaussian Splatting (Kerbl et al., 2023) - Score: 89/145
5. Memory-based NeRFs (Fridovich-Keil et al., 2022) - Score: 86/145
6. Neural Radiance Fields (Mildenhall et al., 2021) - Score: 72/145
7. Filtered Back-projection (Würfl et al., 2016)- Excluded
8. Evolutionary Algorithms (Bartz-Beielstein et al., 2014) - Excluded
9. Graph Neural Networks (Wu et al., 2021) - Excluded
10. Recurrent Neural Networks (Hochreiter and Schmidhuber, 1997) - Excluded
11. Generative Adversarial Networks (Goodfellow et al., 2020) - Excluded

The five highest scoring methods, based on the literature review, were implemented and tested in the project. The methods Gaussian Splatting and memory-based NeRFs generated best results in first tests and were thus selected as focus architectures for this research.

Appendix C. Configuration options for the data generator

The data generator requires the following configuration options. The first set of options are general options and include:

1. the area where the scenario takes place in coordinates in a specified coordinate reference system,
2. the time frame in which the scenario takes place.

The second set of options are required to generate the road network:

1. the number of nodes to be generated and a distribution for their connectivity,
2. the amount of nodes that will the uniformly distributed in the area,
3. a list of node clusters of configurable sizes where the remaining nodes will be placed,
4. the amount of gateways on the boarder of the area where people can escape and how long it takes from there to an emergency center,
5. up to three warning zones: one for take intake of iodine tablets, one for the recommendation to stay inside and one for the recommendation to evacuate, each either given as an area and time frame, by a shape file, or randomly generated.

The thirst set of options are required to generate movement profiles:

1. the number of movement profiles,
2. a distribution of age groups for the generated people,
3. a distribution of group sizes in which the people move (the first person in each group is always an adult),
4. the probability for a person to put on a protective mask,
5. the probability for a person to take an iodine tablet, split by age group, and potential warning zone the person is in,
6. an exploration probability that determines if a person tries to get to an emergency station or just moves randomly inside the road network,
7. a time segment length that describes the maximum duration after which a person potentially changes what they are currently doing,
8. the speed of a person and how much it can change during a new movement decision,
9. residential information like how likely the person is to be outside, in a house or even in a basement, given by their current state, the time of day and the presence of a specific warning zone,
10. how much a person tries to avoid a warning zones when moving,
11. two performance tuning options: a batch size, which is a technical parameter that describes how many movement profiles are generated per iteration of the generator and a greed option for the shortest path algorithm.

Appendix D. Additional figures

Additional figures on reconstruction quality at different resolutions, of different scenarios, with and without prior scenario and with erroneous input data (see Figs. D.4–D.9).

Data availability

The complete code, including the data synthesizer, will be made publicly available as stated in Appendix A.

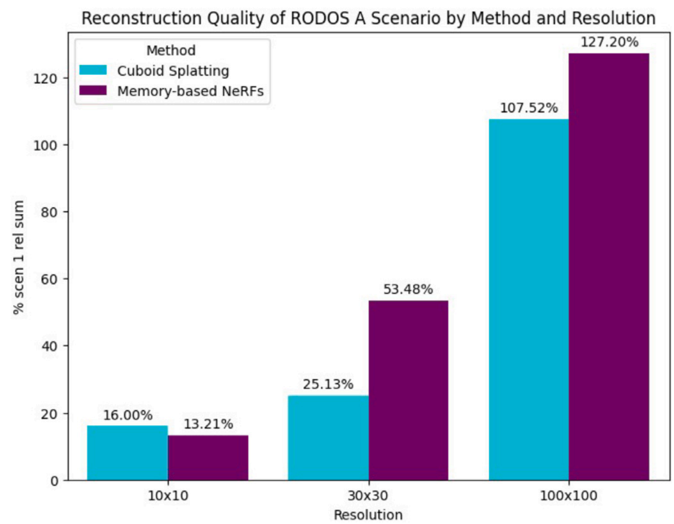

Fig. D.4. Best achieved scenario errors of reconstructing *RODOS A* scenario with both methods by resolution.

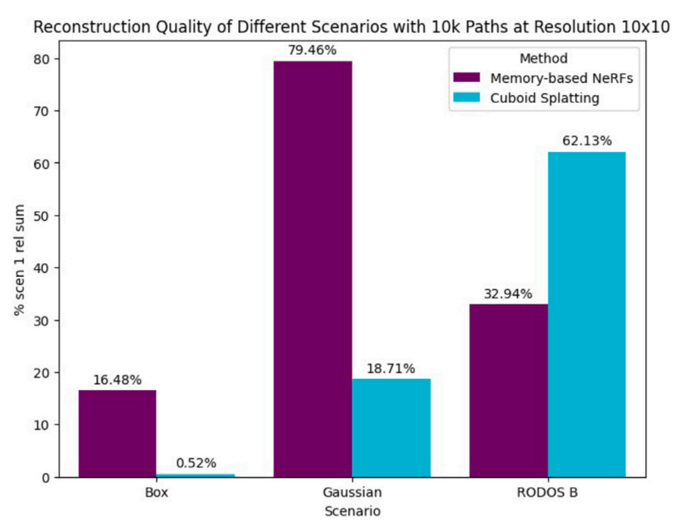

Fig. D.5. Scenario errors of reconstructing different scenarios with 10.000 paths at 10×10 resolution with both methods.

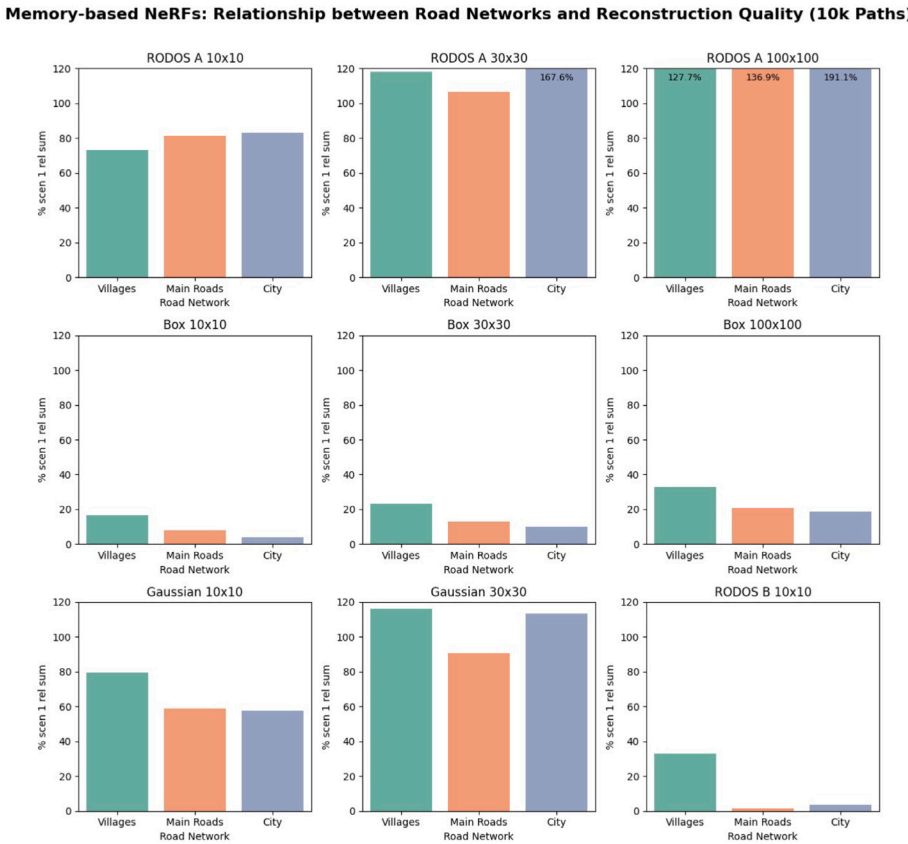

Fig. D.6. Scenario errors of the method memory-based NeRFs applied to multiple combinations of scenarios in different resolutions and three different road networks.

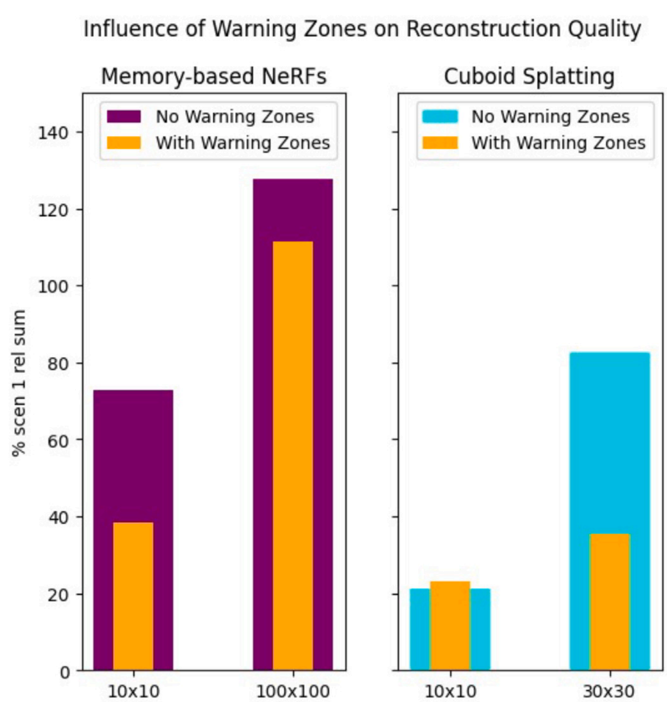

Fig. D.7. Scenario errors of memory-based NeRFs and Cuboid Splatting for the Emsland scenario in different resolutions, with and without warning zones in the same road network.

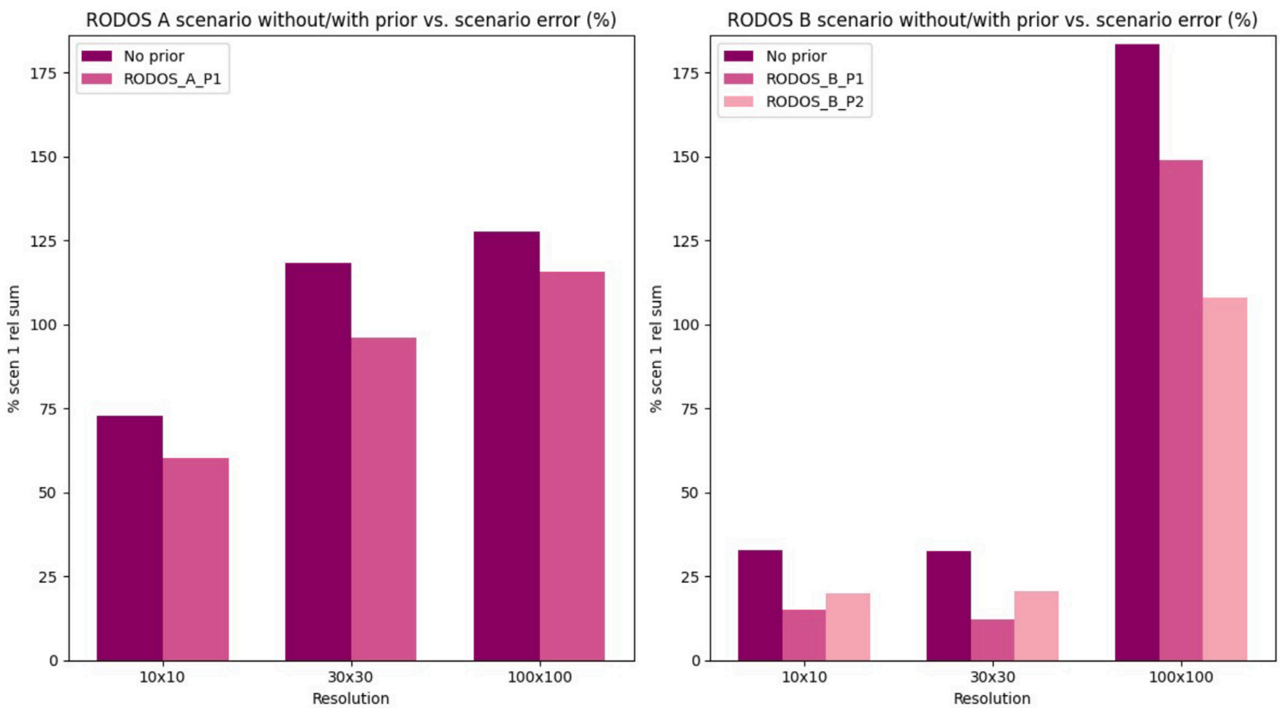

Fig. D.8. Comparison of reconstruction quality without and with prior scenario for the method memory-based NeRFs. Priors lead to lower scenario errors.

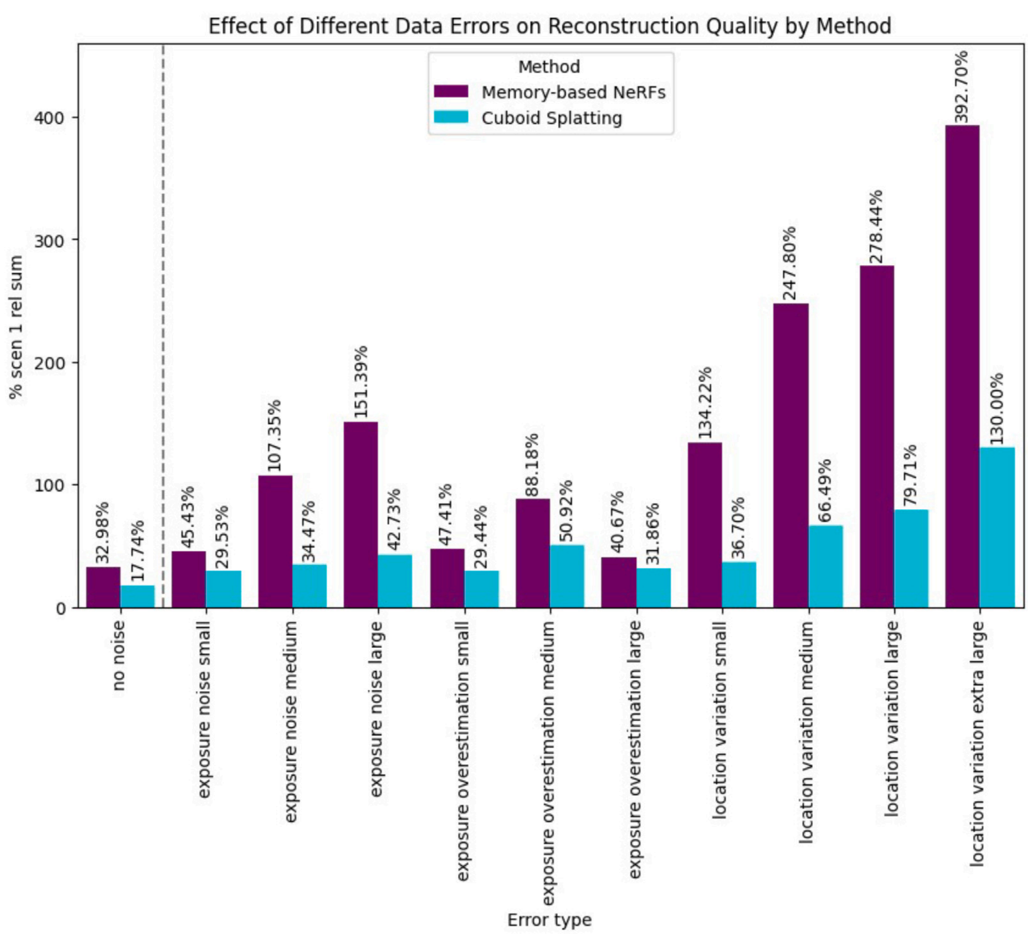

Fig. D.9. Visualization of the effects of different types of errors and intensities on reconstruction quality with both methods. All experiments on *RODOS A* scenario, 25.000 paths, 10×10 resolution.

References

Akhavi Zadegan, A., Vivet, D., Hadachi, A., 2025. Challenges and advancements in image-based 3D reconstruction of large-scale urban environments: a review of deep learning and classical methods. Front. Comput. Sci. 7, 1467103. http://dx.doi.org/10.3389/fcomp.2025.1467103.

Barron, J.T., Mildenhall, B., Tancik, M., Hedman, P., Martin-Brualla, R., Srinivasan, P.P., 2021. Mip-NeRF: A multiscale representation for anti-aliasing neural radiance fields. In: Proceedings of the IEEE/CVF International Conference on Computer Vision. ICCV, pp. 5855–5864. http://dx.doi.org/10.1109/ICCV48922.2021.00580.

Barron, J.T., Mildenhall, B., Verbin, D., Srinivasan, P.P., Hedman, P., 2022. Mip-NeRF 360: Unbounded anti-aliased neural radiance fields. In: Proceedings of the IEEE/CVF Conference on Computer Vision and Pattern Recognition. CVPR, pp. 5470–5479. http://dx.doi.org/10.1109/CVPR52688.2022.00539.

Bartz-Beielstein, T., Branke, J., Mehnen, J., Mersmann, O., 2014. Evolutionary algorithms. Wiley Interdiscip. Rev.: Data Min. Knowl. Discov. 4 (3), 178–195. http://dx.doi.org/10.1002/widm.1124.

Bexon, A., Andronopoulos, S., Croüail, P., Prieto, M.M., Oughton, D., Raskob, W., Turcanu, C., 2023. The NERIS roadmap: research challenges in emergency preparedness, response and recovery. Radioprotection 58 (3), 169–180. http://dx.doi.org/10.1051/radiopro/2023019.

Boyd, S., Boyd, S.P., Vandenberghe, L., 2004. Convex Optimization. Cambridge University Press.

Dashti, M., Stuart, A.M., 2017. The Bayesian approach to inverse problems. In: Ghanem, R., Higdon, D., Owhadi, H. (Eds.), Handbook of Uncertainty Quantification. Springer International Publishing, Cham, pp. 311–428. http://dx.doi.org/10.1007/978-3-319-12385-1_7.

Fojcíková, E., Lipták, L., Krpelanová, M., Chylỳ, M., Čarnỳ, P., 2019. ESTE—Decision support system for nuclear and radiological accidents. Radiat. Prot. Dosim. 186 (2–3), 321–325. http://dx.doi.org/10.1093/rpd/ncz226.

Fridovich-Keil, S., Yu, A., Tancik, M., Chen, Q., Recht, B., Kanazawa, A., 2022. Plenoxels: Radiance fields without neural networks. In: Proceedings of the IEEE/CVF Conference on Computer Vision and Pattern Recognition. CVPR, pp. 5501–5510.

German Commission on Radiological Protection, 2014. Basic Radiological Principles for Decisions on Measures for the Protection of the Population against Incidents involving Releases of Radionuclides. Technical Report, German Commission on Radiological Protection, Bonn, Germany, URL: http://nbn-resolving.de/urn:nbn:de:101:1-201412088183.

German Commission on Radiological Protection, 2015. Weiterentwicklung des Notfallschutzes durch Umsetzen der Erfahrungen aus Fukushima (in English; Further Development of Emergency Preparedness by Implementing Lessons Learned from Fukushima). Technical Report, Bonn, Germany, URL: https://d-nb.info/1080509488/34.

German Commission on Radiological Protection, 2019. Einsatz partikelfiltrierender Halbmasken im Notfallschutz (in German); Use of Particle-Filtering Half Masks in Emergency Protection. Technical Report, German Commission on Radiological Protection, Bonn, Germany, URL: http://nbn-resolving.de/urn:nbn:de:101:1-2020020311302777314573.

Goodfellow, I., Pouget-Abadie, J., Mirza, M., Xu, B., Warde-Farley, D., Ozair, S., Courville, A., Bengio, Y., 2020. Generative adversarial networks. Commun. ACM 63 (11), 139–144. http://dx.doi.org/10.1145/3422622.

Hochreiter, S., Schmidhuber, J., 1997. Long short-term memory. Neural Comput. 9 (8), 1735–1780. http://dx.doi.org/10.1162/neco.1997.9.8.1735.

Hoe, S., McGinnity, P., Charnock, T., Gering, F., Jacobsen, L.H.S., Sørensen, J.H., Andersson, K.G., Astrup, P., 2009. ARGOS decision support system for emergency management. In: 12th International Congress of the International Radiation Protection Association. Online, Argentine Radiation Protection Society.

ICRP, 1995. Age-dependent doses to members of the public from intake of radionuclides - Part 4 inhalation dose coefficients. ICRP Publication 71. Ann. ICRP 25 (3–4), http://dx.doi.org/10.1016/S0146-6453(00)80008-1.

ICRP, 2020. Radiological protection of people and the environment in the event of a large nuclear accident: update of ICRP Publications 109 and 111. ICRP Publication 146. Ann. ICRP 49 (4), http://dx.doi.org/10.1177/0146645320952659.

International Atomic Energy Agency, 2024. Generic Procedures for Medical Response During a Nuclear or Radiological Emergency. Technical Report, International Atomic Energy Agency, Vienna, Austria.

Ishikawa, T., Sorimachi, A., Arae, H., Sahoo, S.K., Janik, M., Hosoda, M., Tokonami, S., 2014. Simultaneous sampling of indoor and outdoor airborne radioactivity after the Fukushima Daiichi nuclear power plant accident. Environ. Sci. Technol. 48 (4), 2430–2435. http://dx.doi.org/10.1021/es404691m.

Jung, J., Han, J., An, H., Kang, J., Park, S., Kim, S., 2024. Relaxing accurate initialization constraint for 3D Gaussian splatting. http://dx.doi.org/10.48550/arXiv.2403.09413, arXiv preprint.

Kerbl, B., Kopanas, G., Leimkühler, T., Drettakis, G., 2023. 3D Gaussian splatting for real-time radiance field rendering. ACM Trans. Graph. 42 (4), http://dx.doi.org/10.1145/3592433.

Kingma, D.P., Ba, J., 2015. Adam: A method for stochastic optimization. In: Bengio, Y., LeCun, Y. (Eds.), 3rd International Conference on Learning Representations, ICLR 2015, San Diego, CA, USA, May 7–9, 2015, Conference Track Proceedings. http://dx.doi.org/10.48550/arXiv.1412.6980.

Liu, L., Gu, J., Zaw Lin, K., Chua, T.S., Theobalt, C., 2020. Neural sparse voxel fields. In: Larochelle, H., Ranzato, M., Hadsell, R., Balcan, M., Lin, H. (Eds.), In: Advances in Neural Information Processing Systems, vol. 33, Curran Associates, Inc., pp. 15651–15663, URL: https://proceedings.neurips.cc/paper/2020/file/b4b758962f17808746e9bb832a6fa4b8-Paper.pdf.

Löffler, H., Mildenberger, O., Sogalla, M., Stahl, T., 2012. Update of the Source Term Catalog of the Decision Support System RODOS for Events During Power Operation (in German, Aktualisierung der Quelltermbibliothek des Entscheidungshilfesystems RODOS für Ereignisse im Leistungsbetrieb). Technical Report, Gesellschaft für Anlagen- und Reaktorsicherheit, Salzgitter, Germany.

Loshchilov, I., Hutter, F., 2019. Decoupled weight decay regularization. In: International Conference on Learning Representations. http://dx.doi.org/10.48550/arXiv.1711.05101.

Mildenhall, B., Srinivasan, P.P., Tancik, M., Barron, J.T., Ramamoorthi, R., Ng, R., 2021. NeRF: representing scenes as neural radiance fields for view synthesis. Commun. ACM (1), 99–106. http://dx.doi.org/10.1145/3503250.

Müller, T., Evans, A., Schied, C., Keller, A., 2022. Instant neural graphics primitives with a multiresolution hash encoding. ACM Trans. Graph. 41 (4), 1–15. http://dx.doi.org/10.1145/3528223.3530127.

Ohba, T., Ishikawa, T., Nagai, H., Tokonami, S., Hasegawa, A., Suzuki, G., 2020. Reconstruction of residents' thyroid equivalent doses from internal radionuclides after the Fukushima Daiichi nuclear power station accident. Sci. Rep. 10 (1), e3639. http://dx.doi.org/10.1038/s41598-020-60453-0.

Paszke, A., Gross, S., Massa, F., Lerer, A., Bradbury, J., Chanan, G., Killeen, T., Lin, Z., Gimelshein, N., Antiga, L., Desmaison, A., Kopf, A., Yang, E., DeVito, Z., Raison, M., Tejani, A., Chilamkurthy, S., Steiner, B., Fang, L., Bai, J., Chintala, S., 2019. PyTorch: An imperative style, high-performance deep learning library. In: Advances in Neural Information Processing Systems 32. Curran Associates, Inc., pp. 8024–8035, URL: http://papers.neurips.cc/paper/9015-pytorch-an-imperative-style-high-performance-deep-learning-library.pdf.

Raskob, W., Landman, C., Trybushnyi, D., 2016. Functions of decision support systems (JRodos as an example): overview and new features and products. Radioprotection 51 (HS1), 9–11. http://dx.doi.org/10.1051/radiopro/2016015.

Raskob, W., Trybushnyi, D., Ievdin, Y., M. Zheleznyak, M., 2011. JRODOS: Platform for improved long term countermeasures modelling and management. Radioprotection 46 (6), 731–736. http://dx.doi.org/10.1051/radiopro/20116865s.

Rodríguez-Lira, D.C., Córdova-Esparza, D.M., Terven, J., Romero-González, J.A., Alvarez-Alvarado, J.M., González-Barbosa, J.J., Ramírez-Pedraza, A., 2025. Recent developments in image-based 3D reconstruction using deep learning: Methodologies and applications. Electronics 14 (15), http://dx.doi.org/10.3390/electronics14153032.

Rojas-Palma, C., Madsen, H., Gering, F., Puch, R., Turcanu, C., Astrup, P., Müller, H., Richter, K., Zheleznyak, M., Treebushny, D., et al., 2003. Data assimilation in the decision support system RODOS. Radiat. Prot. Dosim. 104 (1), 31–40. http://dx.doi.org/10.1093/oxfordjournals.rpd.a006160.

Rückert, D., Wang, Y., Li, R., Idoughi, R., Heidrich, W., 2022. NeAT: neural adaptive tomography. ACM Trans. Graph. 41 (4), http://dx.doi.org/10.1145/3528223.3530121.

Stein, A.F., Draxler, R.R., Rolph, G.D., Stunder, B.J., Cohen, M.D., Ngan, F., 2015. NOAA's HYSPLIT atmospheric transport and dispersion modeling system. Bull. Am. Meteorol. Soc. 96 (12), 2059–2077. http://dx.doi.org/10.1175/BAMS-D-14-00110.1.

Stohl, A., 2006. Characteristics of atmospheric transport into the arctic troposphere. J. Geophys. Res.: Atmos. 111 (D11), http://dx.doi.org/10.1029/2005JD006888.

United Nations Scientific Committee on the Effects of Atomic Radiation, 2014. UNSCEAR 2013 Report, Volume I, Scientific Annex A: Levels and Effects of Radiation Exposure Due to the Nuclear Accident After the 2011 Great East-Japan Earthquake and Tsunami. Technical Report, United Nations Scientific Committee on the Effects of Atomic Radiation, New York, USA, URL: https://www.unscear.org/unscear/en/publications/2013_1.html.

United Nations Scientific Committee on the Effects of Atomic Radiation, 2022a. UNSCEAR 2020/2021 Report, Volume II, Annex B, Attachment A-2: The Estimation of Thyroid Doses Resulting from the Accident at the Fukushima Daiichi Nuclear Power Station and Their Validation. Technical Report, United Nations Scientific Committee on the Effects of Atomic Radiation, New York, USA, URL: https://www.unscear.org/unscear/en/publications/2020_2021_2.html.

United Nations Scientific Committee on the Effects of Atomic Radiation, 2022b. UNSCEAR 2020/2021 Report, Volume II, Annex B: Levels and Effects of Radiation Exposure Due to the Accident at the Fukushima Daiichi Nuclear Power Station: Implications of Information Published Since the UNSCEAR 2013 Report, Appendix A: Assessment of Doses to the Public. Technical Report, United Nations Scientific Committee on the Effects of Atomic Radiation, New York, USA, URL: https://www.unscear.org/unscear/en/publications/2020_2021_2.html.

Vanderbei, R.J., et al., 2020. Linear Programming. Springer.

Verger, P., Aurengo, A., Geoffroy, B., Le Guen, B., 2001. Iodine kinetics and effectiveness of stable iodine prophylaxis after intake of radioactive iodine: a review. Thyroid 11 (4), 353–360. http://dx.doi.org/10.1089/10507250152039082.

Wu, Y., Zhuang, D., Labbe, A., Sun, L., 2021. Inductive graph neural networks for spatiotemporal kriging. In: Proceedings of the AAAI Conference on Artificial Intelligence, vol. 35, (no. 5), pp. 4478–4485. http://dx.doi.org/10.1609/aaai.v35i5.16575.

Würfl, T., Ghesu, F.C., Christlein, V., Maier, A., 2016. Deep learning computed tomography. In: Ourselin, S., Joskowicz, L., Sabuncu, M.R., Unal, G., Wells, W. (Eds.), Medical Image Computing and Computer-Assisted Intervention. MICCAI 2016, Springer, pp. 432–440. http://dx.doi.org/10.1007/978-3-319-46726-9_50.

Zaletel, K., Mihovec, A., Gaberscek, S., 2024. Characteristics of exposure to radioactive iodine during a nuclear incident. Radiol. Oncol. 58 (4), 459–468. http://dx.doi.org/10.2478/raon-2024-0051.